Nanoscale Res Lett (2007) 2:219–229
DOI 10.1007/s11671-007-9056-6

NANO REVIEW

Nanoscale waveguiding methods

Chia-Jean Wang · Lih Y. Lin

Received: 12 March 2007 / Accepted: 30 March 2007 / Published online: 1 May 2007

Abstract While 32 nm lithography technology is on the horizon for integrated circuit (IC) fabrication, matching the pace for miniaturization with optics has been hampered by the diffraction limit. However, development of nanoscale components and guiding methods is burgeoning through advances in fabrication techniques and materials processing. As waveguiding presents the fundamental issue and cornerstone for ultra-high density photonic ICs, we examine the current state of methods in the field. Namely, plasmonic, metal slot and negative dielectric based waveguides as well as a few sub-micrometer techniques such as nanoribbons, high-index contrast and photonic crystals waveguides are investigated in terms of construction, transmission, and limitations. Furthermore, we discuss in detail quantum dot (QD) arrays as a gain-enabled and flexible means to transmit energy through straight paths and sharp bends. Modeling, fabrication and test results are provided and show that the QD waveguide may be effective as an alternate means to transfer light on sub-diffraction dimensions.

Keywords Nanophotonics · Negative dielectric · Waveguides · Quantum dots · Diffraction limit

C.-J. Wang (✉) · L. Y. Lin
Department of Electrical Engineering, University of Washington, Box 352500, Seattle, WA 98195, USA
e-mail: jeanwang@u.washington.edu

L. Y. Lin
e-mail: lylin@u.washington.edu

1 Introduction

Discovering ways of guiding light on the nanoscale together with the corresponding logic components is the key to developing a range of highly integrated and compact photonic chips. In addition, there is growing interest for reducing the size and enhancing speed of transfer at the optical-electrical interface. Still, the main issue of preventing undue loss and limiting the optical mode width to below that of the transmitting wavelength is a bottleneck for progress. Over the past few decades, a number of inventive means have been proposed and are gaining momentum due to the increasing sophistication of fabrication capabilities. Specifically, nanotechnology-related tools enable and help create metal, semiconductor and silica structures designed to become part of the foundation for future optical circuits. The aim of the article is to highlight devices positioned to fulfill the waveguide niche.

In particular, Sect. 2 addresses the theoretical background, formation and experimental results of existing negative dielectric (ND) based sub-micrometer waveguides. Three categories of related devices are discussed such that Sect. 2.1 provides an overview of metallized optical fibers, Sect. 2.2 relates to metal as the central waveguiding region, and Sect. 2.3 to metal slot-type waveguides. Next, Sect. 3 presents nanoribbon, silicon-on-insulator (SOI) high-index-contrast and photonic crystal methods for forming structures that propagate optical waves. The three techniques covered in sequential subsections may be considered large scale in sub-diffraction methods. In Sect. 4, a gain-enabled way for waveguiding through quantum dot (QD) arrays is explored in detail with subsections devoted to the QD model, waveguide fabrication and test results. The review concludes in Sect. 5 with a summary of discussed devices and future directions.

2 Waveguiding with negative dielectric materials

Numerous sub-diffraction propagation techniques rely on ND materials such as gold or silver to suppress loss and enable two or one-dimensional waveguiding. Here, we delve into the fundamentals of three devices in which metal serves different functions, namely, as either the transmitting or confining medium for electromagnetic propagation.

2.1 Negative dielectric optical fibers

The ND waveguide and its theory is the cornerstone for using metal as an integral part of optical propagation. Takahara et al. first proposed a 1D waveguide [1] by noting that the ND property of metal removes the conventional restraints:

$$\begin{aligned} &0 < \varepsilon_{\text{clad}} < \varepsilon_{\text{core}}, \\ &\beta, k_y, k_z, \kappa_y, \kappa_z \leq \tfrac{\omega}{c}\sqrt{\varepsilon_{\text{dielec}}} \end{aligned} \tag{1}$$

given $\varepsilon_{\text{core}}$, $\varepsilon_{\text{clad}}$ are the dielectric constants, k_y and k_z are the wave vectors inside the core and κ_y and κ_z are those for the cladding. Instead, the y and z components become imaginary and evanescent thus limiting propagation to the x direction and breaking the upper bound limit for beam diameter. Several types of ND structures, formed by curling a 2D waveguide into a cylinder, are depicted in Fig. 1.

The wave solutions of the 1D propagators are found to be modified Bessel functions. Deducing the phase constant and beam radius relation with respect to the core radius, the simulation [1] shows no cutoff in the core size and is continuous over all radii as revealed for the lowest order mode, TM_{01}. Focusing on the pin formation (Fig. 1a), transmission loss at 633 nm wavelength is calculated to be 3 dB/410 nm or 7.3 dB/μm for a silver core of 20 nm diameter($\varepsilon_{r,\text{Ag}}$ = –19–0.53i) clad by a dielectric ($\varepsilon_{r,\text{dielec}}$ = 4). The diminishing signal is directly caused by the imaginary portion of the core dielectric and is physically realized through dissipative heating effects.

Fabrication of a one-dimensional ND waveguide remains elusive as creating smooth metal films on nanometer size dielectric fibers or encasing a metal core with dielectric is difficult. Integration of a nanowire to a system also presents a challenge in nanoscale manipulation. Still, there are a number of devices for 2D sub-diffraction guiding, which are discussed in the next two sections.

2.2 Metal strips, wedges and nanoparticle arrays

The simplest case for utilizing ND material to guide light is to rely on the induced dipole oscillation effect at the surface of the metal, which creates plasmons that interact in a coherent fashion to propagate energy downstream. Such coupling, which gives rise to surface plasmon polaritons (SPP), has a limited propagation length caused by resistance inherent to the material leading to radiative loss and wave decay in directions perpendicular to the interface.

The basic form of the waveguide, depicted in Fig. 2a is the metal strip. A thin nanowire is built on a substrate and may be inserted in between dielectric or left standing in air. Experimental work for a 200 nm wide, 50 nm thick gold strip confirms TM mode guiding of 800 nm wavelength light, which is clearly below the diffraction limit [2]. The propagation length, or the distance at which intensity drops to 1/e of the incident value, is measured with the aid of a photon scanning tunneling microscope to be 2.5 μm, consistent with 1.7 dB/μm. Contrasting a 20 μm with a 8 μm long waveguide, Krenn et al. [2] also discovered resonant behavior in intensity along the length for the shorter structure due to scatter and reflection behavior at the edges.

A similar device, shown in Fig. 2b, is the metallic wedge [3]. With the aid of 3D finite-difference time domain (FDTD) software, a new wedge-plasmon (WP) eigenmode is realized at the tip of the triangular shape and interferes with the SPPs on the sides. Notably, when the wedge angle is less than 30°, more WP modes are supported. End-fire coupling 632 nm light to a silver coated wedge of 40° with ~300 nm base yields 1.5 μm propagation length (2.9 dB/μm) as detected by a near-field optical

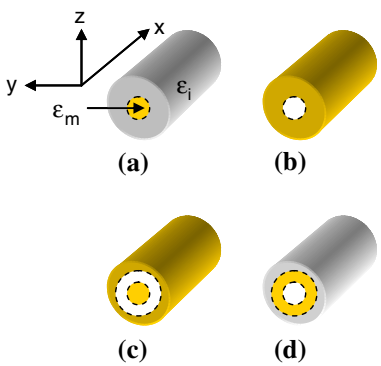

Fig. 1 ND waveguides: (**a**) pin, (**b**) hole, (**c**) coaxial, and (**d**) tube formations

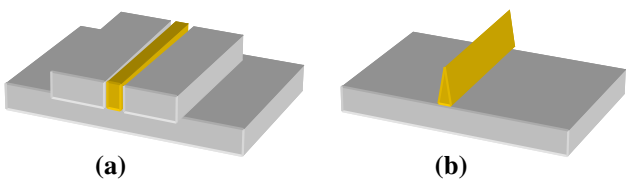

Fig. 2 (**a**) Metal strip (surrounding dielectric is optional) and (**b**) wedge waveguides

microscope (NSOM). As theoretical prediction of the propagation length yielded 2.25 μm (1.9 dB/μm), roughness of the metal at the tip, variations between the optical properties of metal films and bulk, and changes in the silver film caused by the focused ion beam fabrication technique are considered to be the culprits for the deviation.

Perhaps the most popular ND method is the metal nanoparticle waveguide. A basic example, as illustrated in Fig. 3, consists of an evenly spaced array nominally formed by using e-beam lithography to define nanoscale holes in a polymer-resist coated substrate. Thermal evaporation of silver or gold onto the sample followed by liftoff of the resist produces the waveguide.

First proposed by Quiten, Leitner, Krenn and Aussenegg, Mie theory was used to model guiding by a linear chain of 50 nm diameter silver particles [4]. At the most favorable inter-dot distance, the plasmons oscillate constructively at resonance to improve transfer. By the same token, resistive loss is maximized and as the waveguide cross-section, defined by the nanoparticle diameter, decreases, the mode is confined to a smaller degree. Searching for an optimal spatial distribution of the nanoparticles at 488 nm wavelength to approach the 380 nm resonance peak of Ag, 25 nm separation produced the highest electromagnetic transfer with 900 nm propagation length (4.8 dB/μm). The model for plasmon transfer was further extended by Brongersma et al. to calculate efficiencies of transverse and longitudinal waves at junctions and 90° bends in the placement of metal nanodots [5].

A convincing demonstration of guiding with the nanoparticle arrays was carried out by Maier et al. through NSOM probe pumping of an array interspersed with dye molecules [6]. In localizing the excitation spot, subsequent appearance of fluorescence without increase of the full-width half maximum profile along the linear chain indicated energy transfer. Attenuation lengths were calculated to be 200 and 30 dB/μm for 50 nm diameter Au and Ag particles, the latter of which was confirmed through experiment.

From the other side, by designing arrays whose nanoparticles are closer in proximity, strong confinement of the field may be achieved [7]. With 10 nm diameter Ag NPs and separation varied from 0 to 4 nm, confinement measured at the center of four dots increases by nearly a factor of 100 for 1–2 nm spacing compared to that at 4 nm. Furthermore, there is a red shift found in simulation of the extinction spectra for an increase in separation or number of particles. The two points indicate that at small NP count, the model and measured outcome are strongly affected by each incremental addition and spacing between particles. Such trends will tend to decrease in magnitude with longer arrays.

As a means to both create a fiber-accessible device and decrease the thermal loss, a 2D array of metal nanoparticles is proposed. Indicated by the red shift for strongly coupled NPs, the resonance frequency of a collection of dots will shift slightly below resonance with respect to the individual NP. Monitoring the transmission of 1,600 nm wavelength light from a fiber taper to the array shows up to 75% power transfer for a square lattice with 500 nm pitch [8].

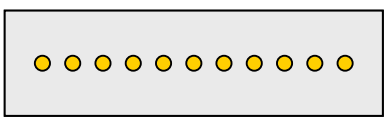

Fig. 3 Metal nanoparticle array

2.3 Metal slot waveguides

Instead of using metal as the central part of the waveguide, a metal-encased structure (in Fig. 4) is an alternative method to exploit SPP to propagate optical frequency waves. Since energy transfer depends on the metal to dielectric interface interaction, SPPs exist in the slot configuration.

To permit sub-diffraction guiding, a lower bound on the wave vector may be derived from the wave equation to give [9]:

$$k_z \geq \frac{\omega}{c}\sqrt{2\varepsilon_{\text{dielec}}}, \tag{2}$$

which is only met near the plasmon resonance frequency. Secondly, to ascertain the decay length into the metal sides, the following relation must also be valid:

$$\Re(\varepsilon_{\text{metal}}) < -\varepsilon_{\text{dielec}} \quad \rightarrow$$
$$\frac{2\pi n_{\text{dielec}}}{\lambda} < \frac{\omega}{c}\sqrt{2\varepsilon_{\text{dielec}}} = \frac{2\sqrt{2}\pi n_{\text{dielec}}}{\lambda} < \left|k_{x,\text{metal}}\right|. \tag{3}$$

Equations 2 and 3 imply that propagation may occur inside the slot at the cost of non-negligible attenuation into the metal. In fact, metal slot waveguides can be more effective than the metal strip in terms of coupling and confinement of the transverse mode, but propagation length becomes a tradeoff as a larger part of the field reacts with the lossy metal and experience higher decay of the field. Hence, the slot distance, d, which is proportional to mode confinement, has an inverse relation to the propagation length.

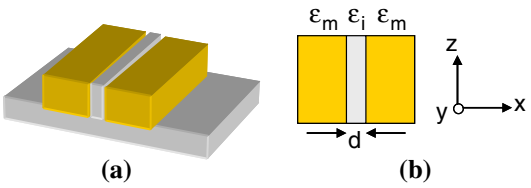

Fig. 4 Metal slot waveguide: (**a**) 3D view and (**b**) bird's eye view

Defining a confinement factor as the ratio between the power inside the center region to that over all space, and propagation length, comparisons may be drawn between the metal slot (MIM) to the metal strip (IMI) waveguide [9]. Simulation results show that propagation length increases from ~5 μm (d = 45 nm) to 125 μm (d ~ 10 μm) for MIM and drops from 6 mm (d = 45 nm) to 125 μm (d ~ 200 nm) for IMI devices. Translating to loss, the minimum values roughly correspond to 0.860 dB/μm (d = 45 nm) 0.034 dB/μm (d = 10 μm) for MIM and 7.6×10^{-4} dB/μm (d = 45nm) 0.034 dB/μm (d = 200 nm) for IMI. With regards to confinement, MIM structures are found to be confined four orders of magnitude more than IMI so that 99% of the mode is captured in the slot starting at 45 nm while a maximum of ~0.01% is enclosed within strip guides 25 nm and wider.

Of late, experimental results for metal slot devices reveal the efficacy of the method using gold and silver [10, 11]. In the case for the most narrow slot distance waveguide, Chen et al. reported a loss of ~0.8 dB/μm where theory predicts 0.55 dB/μm for a 150 nm wide and 250 nm thick Si center set inside gold on a silicon dioxide substrate with a 80 nm SiO_2 capping layer to insulate the wave from top-side gold (see Fig. 5).

Moreover, a variation of the metal slot device exists, such that the refractive index of middle dielectric is graded [12, 13]. Modeling both constant index and index-graded structures for an index- guided thickness of 100 nm and a center SiO_2 width of 150 nm at and λ = 633 nm, loss is determined to be 12.2 dB/μm and 3.10 dB/μm, respectively [12]. The gap, sandwiched by two gold layers, consists of air-SiO_2-air so that the refractive index varies from 1 to 1.455 back to 1.

Besides the metallic structures discussed above, some hybrid, newer waveguides have been proposed and in some cases, fabricated. Specifically, the inclusion of gold peapods (nanoparticles) in a silica nanowire (NW) allows direct optical modulation of conductivity [14]. The largest variation occurs at the resonance frequency of the gold NPs near 532 nm. Contrasting with a plain silica NW, the altered one has a nominal resistance of ~42 kΩ, which is six times less due to the gold, but notably shows a stark contrast in resistivity as pump light is turned on and off. At resonance, there is a 10 kΩ change and away from the peak wavelength, the excursion reduces to ~3kΩ.

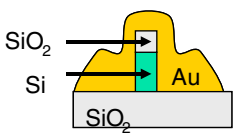

Fig. 5 Cross-section of metal slot waveguide [10]

Another method clads a carbon nanotube of 50 nm radius surrounded by aluminum dioxide 100 nm thick with 50 nm of chrome. The result is a visible light sub-diffraction waveguide that may also act as a nanoantenna by extrusion of the inner electrode [15]. Although loss is not quantified, it is estimated that the propagation length is 50 μm (0.086 dB/μm) owing to the coaxial technique, like that originating from Takahara, which enables higher propagation through impedance matching. To conclude the section, a metal clad gain-enabled semiconductor core waveguide has been suggested [16]. As expected, there is a compensatory relation between gain and propagation length as a function of the core diameter. For 1500 nm wavelength transmission, lossless propagation is found to be theoretically possible for a core of 50 nm and gain of 4830 cm^{-1}.

Overall, 2D ND waveguiding is not without cost. Improving the loss figure and propagation length is at the mercy of increased device width and mode confinement. The resistive component of metals, lack of conversion mechanisms between electrical, optical and plasmon energy and the irregularities of fabrication contributing to non-ideal mode profiles are continuing issues. Tradeoffs must be balanced to enable sub-diffraction propagation in the ND regime.

3 Sub-Micrometer transmission techniques

In addition to plasmonic excitation for energy transfer, there are several additional methods that rely on semiconductor materials. The first two discussed in the section operate on the premise of confining a wave by index contrast between core and cladding-type media; however, the third is based on optical bandgap control. While the active structure is generally sub-micrometer, there is a minimum size limit for all three devices and leakage of the mode between adjacent structures is a key issue. Therefore, the methods mentioned here, while nanoscale, are not under sub-diffraction limit dimensions.

3.1 The Nanoribbon

Recently, waveguiding from nanoscale crystals grown into ribbon shape from SnO_2 and ZnO have been demonstrated [17, 18]. Modeling the ribbon or wire structure as a cylinder, the cutoff condition [19] and hence the minimum waveguide size can be derived from the boundary matching conditions of electromagnetic waves in core and cladding applied for the lowest mode, n = 0, to permit TE_{01} and TM_{01} propagation. The cutoff frequency is defined as the first non-trivial zero root, u_1, for the Bessel function, J_0, so that:

$$V_c = u_1 = 2.4048 = k_c a\sqrt{n_1^2 + n_2^2}, \quad k_c = 2\pi/\lambda_c \tag{4}$$

where k_c and λ_c are the cutoff wave number and wavelength, a is the radius of the core, n_1 and n_2 are the refractive indices of the core (SnO_2 = 2.1) and cladding (air = 1), respectively.

In the nanoribbon case, the corresponding minimum diameters to support 442, 532 and 652 nm excitation sources are 180 nm, 220 and 270 nm which are reported to fit well with 100–400 nm width and thickness dimensions of the rectangular-like ribbons. By exciting the ribbon at different points along its length with respect to a near-field optical microscope probe, measured losses varied from 1 to 8 dB/mm for 450 and 550 nm wavelengths.

Besides propagation, Law et al. also propose to use the structure in many different functions, namely filters, couplers and photodetectors, to build photonic circuitry. Short-pass filter functionality is defined by limiting the path length traveled by the pump light and discovered through photoluminescence data where longer wavelengths are attenuated faster at shorter distances. On the other hand, coupling and photodetecting operations take advantage of evanescent transfer between two ribbons in contact by van der Waals attraction or aligned face to face. However, scattering losses at surface defects along the nanoribbon work against efficient transfer. Furthermore, although the output intensity is largely preserved under bending with radii of curvature close to 1 μm, the mode profile is seen to change dramatically upon exiting the guide.

3.2 Silicon-on-insulator high-index-contrast waveguide

Waveguides defined by controlling the shape and deposition of core and surrounding medium dielectrics have long been utilized for energy transfer. From Maxwell's equations, we have the cutoff for cylindrical guides given in Eq. (4). The frequency or wavelength cutoff solution provided by the TE_{10} mode for rectangular guides may as easily be found [19]:

$$f_c = \frac{c}{2w\sqrt{n_1^2 - n_2^2}} \rightarrow \lambda_c = 2w\sqrt{n_1^2 - n_2^2}. \tag{5}$$

The width of the high index guide is w and c is the speed of light. Consequently, for a silicon (n = 3.875) wire inside silicon dioxide (n = 1.455) at 1550 nm wavelength, the minimum width is 432 nm, or more generally on the order of 500 nm, to guide at frequencies that are minimally absorbed by Si. The lowest loss reported for a such a Si/SiO_2 strip waveguide is 0.8 dB/cm measured at 1540 nm after various step were taken to smooth the sidewall roughness [20].

Using the strip device as a basis for an active component such as a modulator has also been achieved by adding a p-i-n diode underneath a 425 nm wide by 250 nm thick waveguide to alter the effective index [21]. The modulation speed was measured to be on the order of 1 ns. In addition, the refractive index setup may be inverted where an air- or SiO_2-filled slot is sandwiched between two Si channels to form a low-index waveguide. Simulation and experimental findings for 218 nm wide Si strips separated by 101 nm confirmed a major TE component guided mode in the air channel by observing reduced effective index [22].

Furthermore, CMOS process fabrication of high-index-contrast waveguides results in devices whose losses are 34 dB/mm for 500 nm width and 60 dB/mm for 600 nm width deep-etched devices (in Fig. 6a). However, for removal of only the silicon material (Fig. 6b), the loss may be reduced to 3.4, 0.74, 0.24 dB/mm for 400, 450 and 500 nm width waveguides. The thicknesses of the top Si layer and SiO_2 are 220 nm and 1 um as reported in Ref. 23. With incorporation of smoothing techniques, the loss may be further suppressed.

3.3 Photonic crystal waveguide

Photonic crystals have the advantage of reducing the radiative loss characteristic known in common index-contrast based waveguides due to the optical bandgap confinement. However, as the 3D photonic crystal (PhC) presents a continuing challenge both to fabricate and integrate with optical components, 2D PhCs may be manufactured and tested more readily. Numerous studies have been done to implement PhC waveguides [24, 25], where W1 denotes the basic structure created from a single line defect. For a SiO_2 cladded PhC W1, minimal loss is found to be 1.5 dB/mm, while an alternative air-clad one gave 0.6 dB/mm [26]. Such waveguides have an airhole pitch of 500 nm with a diameter of 220 fabricated within a Si layer thickness of 200 nm. Only the top Si layer is etched.

Furthermore, a study using CMOS technology to create the W1 device demonstrates waveguiding [23]. Using customized SOI wafers and deep UV lithography, periodic

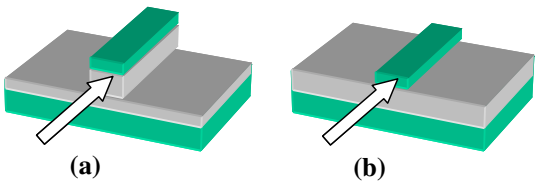

Fig. 6 (**a**) A high-index-contrast and (**b**) deep-etched waveguide built on SOI wafer, light enters in direction of arrow. The waveguide may be further buried under a cladding layer

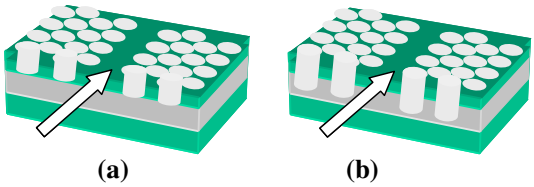

Fig. 7 (**a**) Silicon-only and (**b**) deep-etched photonic crystal waveguide built on SOI wafer, light enters in direction of arrow

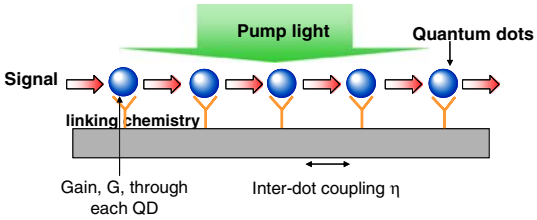

Fig. 8 QD waveguide in operation [46]

holes were etched from the top Si layer and stopped at the buried oxide (Fig. 7a) or for deep-etched devices (Fig. 7b), the hollow was carved through the oxide layer as well. Overall, the lattice pitch is 500 nm with 320 nm hole diameter.

Comparing the minimum losses, Bogaerts et al. measured 7.5 dB/mm for the silicon and 21 dB/mm for deeply-etched structures at 1525 nm wavelength. It is believed that with thermal oxidation, sidewall roughness may be reduced to improve light throughput. Still, photonic crystal methods are highly sensitive to fabrication variations as well as optical proximity effects and require progress in processing equipment to enable an ideal outcome. Furthermore, the required lattice structure to achieve adequate light confinement of PhCs enlarges the total dimension of the waveguide to the order of micrometers.

While techniques in Sect. 3 are nominally restricted to index and bandgap manipulation for optical propagation, it is useful to note that a molecular scale waveguide has been proposed and experimentally verified [27]. Representing a bottom-up approach, transfer of photons through a DNA scaffold using fluorescence resonance energy transfer (FRET) whereby photons are absorbed at higher energy and re-emitted at a longer wavelength in a chain reaction along the DNA length. Certainly, the improvement of atomic level understanding and manipulation will encourage the creation of more transmission devices based on such fundamental components as molecules.

4 Quantum dot array waveguides

In the devices previously discussed, the major unifying characteristic is that all are susceptible to compounded loss effects. Individually, the different techniques may be limited in their applications because of fabrication, integration or energy conversion difficulties. To address the issues, we turn to quantum dots as a source for reducing loss by introducing gain into the system, and manufacturing devices that may be self-assembled to easily scale in the submicron regime.

The QD, which has been widely investigated, has found prominence in biological [28, 29], lasing [30–35] and coupled optical device [36, 37] applications. The properties of emission tunability by varying size [38–40], the effect of QD shape, surface passivation and capping layers [41, 42], the non-radiative recombination processes [43–45] and their respective characterization methods are largely understood. Hence, the QD is an attractive candidate for nanophotonics owing to its versatility and nanometer dimension.

In particular, we examine the application of QDs to waveguide structures. Our proposed device, illustrated by Fig. 8, relies on a pump light to excite electrons into the conduction band to enable gain and a signal light introduced as one edge of the waveguide to generate stimulated emission, which produces photons that cascade through the QDs downstream. The quality of the transmitted light is affected by the gain each QD is capable of yielding as well as the photon coupling efficiency between adjacent particles.

We review the gain and 1D transmission model, delve into the transmission properties of a QD array, and present both fabrication and test processes and results in the ensuing sections.

4.1 Gain modeling

Taking the QD as a box to calculate the corresponding energy states, we may model gain with a three level system [47]. In general, linear gain [48],

$$G(\omega) = \frac{\omega}{n_r}\sqrt{\frac{\mu_0}{\varepsilon_0}}\sum_{lmn}\int_{E_g}^{\infty}\langle \mathbf{R}_{\mathrm{ch}}^2\rangle \frac{g_{\mathrm{ch}}[f_c(E_2)-f_v(E_1)]\hbar/\tau_{\mathrm{in}}}{(E_{\mathrm{ch}}-\hbar\omega)^2+(\hbar/\tau_{\mathrm{in}})^2}dE_{\mathrm{ch}}, \tag{6}$$

is expressed as the net emission subtracted by absorption, which is directly proportional to the quasi-Fermi level in the valence band, f_v, deducted from that of the conduction band, f_c. $\mathbf{R}_{\mathrm{ch}}$ is the dipole moment, n_r is the refractive index, g_{ch} is the QD density of states, τ_{in} is the intraband relaxation time, E_1 and E_2 are quasi-Fermi energies in the conduction and valence bands, and E_g is the QD material bandgap energy. Equation 6 encompasses all excited states denoted by quantum numbers l, m and n, by the

summation of the integral. While most of the variables are defined by the material properties, the quasi-Fermi energies are also dependent on the pump characteristics. Consequently, we must use a self-consistent approach to find E_1 and E_2 [49].

Assuming the excitation comes from an optical source in continuous wave (CW) operation, and the structure is in steady state, we can write the equilibrium equations such that the number of electrons must equal that of holes and the absorption rate balances out all emission processes:

$$N = P \Rightarrow \sum_{lmn} \frac{1}{f_c(E_{clmn})} = \sum_{lmn} \frac{1}{(1 - f_v(E_{hclmn}))}, \tag{7}$$

$$r_{\text{abs},02} = r_{\text{st.ems},20} + r_{\text{sp.ems},20} + r_{\text{sp.ems},10} \tag{8}$$

where we have the electron absorption and stimulated and spontaneous emission rates defined:

$$r_{\text{abs},02} = \frac{P_{\text{pump}}}{\hbar\omega_p}\alpha(\omega_p)L_z, \tag{9}$$

$$r_{\text{st.ems},20} = \frac{P_{\text{pump}}}{\hbar\omega_p}e(\omega_p)L_z, \tag{10}$$

$$r_{\text{sp.ems},10} = \frac{f_c(E_{1e})[1 - f_v(E_{1h})]}{\tau_{10}} \times \int_{Eg}^{\infty} \frac{\hbar/\tau_{10}}{[E - (E_{1e} - E_{1h})]^2 + (\hbar/\tau_{10})^2} dE \tag{11}$$

$$r_{\text{sp.ems},20} = \frac{f_c(E_{2e})[1 - f_v(E_{2h})]}{\tau_{20}} \times \int_{Eg}^{\infty} \frac{\hbar/\tau_{20}}{[E - (E_{2e} - E_{2h})]^2 + (\hbar/\tau_{20})^2} dE \tag{12}$$

with τ_{10} and τ_{20} representing $1 \rightarrow 0$ and $2 \rightarrow 0$ state transition decay times. L_z is the z dimension length of the QD box, on which the pump light at ω_p frequency and power, P_{pump}, impinges. The spontaneous emission rates are modified by Lorenztian broadening to simulate electron–electron collision effects while the absorption and stimulated emission profiles reflect the absorption and emission response at the pump frequency.

The optical pump light on the QD creates a feedback loop where electron-hole (e-h) pairs are first generated, altering the quasi-Fermi energies and hence the quasi-Fermi levels. Accordingly, the absorption and emission behaviors change over the frequency range and for the specific ω_p further influences the rates of absorption and stimulated emission by creating an upper limit due to the finite number of e-h pairs a QD may support. Consequently, the nanocrystal gain behavior is intricately tied to the pump characteristics. As an example, gain spectra for a 7.4 nm × 7.4 nm × 7.4 nm CdSe core with a 2 monolayer or 1.1 nm ZnS shell QD are depicted in Fig. 9 and show increasing gain over 1 pW to 10 nW pump power range for 655 nm emission. Gain saturation, and thus the optimum pump level, occurs at about 1 nW.

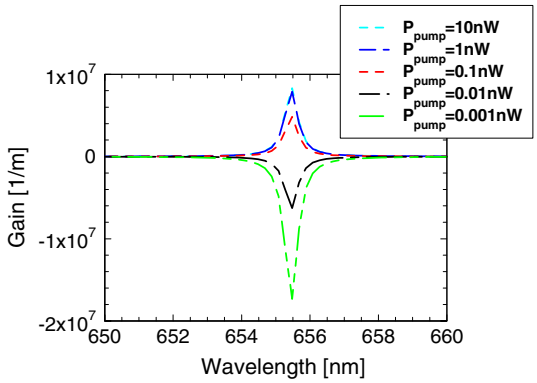

Fig. 9 Gain spectra of a 7.4 nm × 7.4 nm × 7.4 nm CdSe/ZnS quantum cube with CW excitation

Now considering the propagation of light along the QD waveguide, one transmission model exploits the ABCD matrix approach. Described in prior work [49], we may express forward and backward propagating intensities at the exiting edge as a function of the input light transformed by cascaded QD matrices alternating with free space coupling matrices:

$$\begin{bmatrix} I_{\text{out},+} \\ I_{\text{out},-} \end{bmatrix} = M_{\text{QD}} \cdot \left(M_{\text{prop}} \cdot M_{\text{QD}}\right)^{N-1} \cdot \begin{bmatrix} I_{\text{in},+} \\ I_{\text{in},-} \end{bmatrix} \tag{13}$$

$$\text{where } M_{\text{QD}} = \begin{bmatrix} 0 & 1 \\ -1 & 2e^{-G} \end{bmatrix}, \text{ and } M_{\text{prop}} = \begin{bmatrix} \eta & 0 \\ 0 & \eta^{-1} \end{bmatrix}. \tag{14}$$

The QD to QD interaction is denoted by the coefficient, η, to describe the probability that a photon is coupled from one nanocrystal to the next. N is the number of QDs in the 1D array waveguide.

After solving for the forward output relative to the forward input intensity given the backward traveling wave at the exit is zero, we may plot the transmission in terms of the various coupling efficiencies over a gain range. Figure 10 demonstrates the results in relative intensity for a five QD waveguide. Additionally, using FDTD to model crosstalk between two colloidal QD arrays, where the nanocrystal is 10 nm in diameter, shows much less energy transfer compared to 10 nm wide conventional dielectric waveguides at the same separation. At equal crosstalk levels, the QD devices may be spaced more closely at a factor of 0.39 less than 200 nm wide dielectric structures [50].

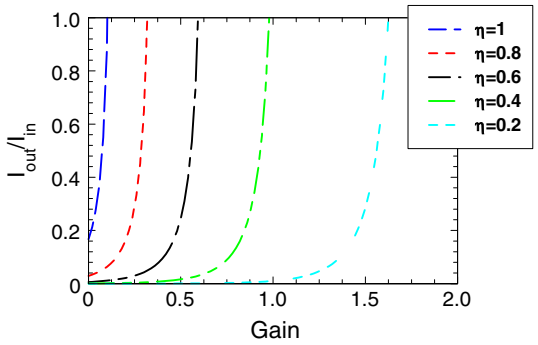

Fig. 10 Relative output for a five QD 1D waveguide

4.2 QD waveguide fabrication

The device may be fabricated through two types of self-assembly processes. A deoxyribonucleic acid assisted technique, discussed in previous works [51], has the advantage of a programmable element founded on the complementary base pairs in double stranded DNA. Briefly, we use e-beam lithography (EBL) to pattern a line on a polymethylmethacrylate (PMMA) coated SiO_2/Si substrate. After development, the sample is primed with hydroxyl groups by oxygen plasma treatment. 3′mercaptopropyltrimethoxysilane (MPTMS) is vapor-phase deposited on the surface and acrydite modified single strand DNA binds to the –SH group. Next, biotinylated complementary strand DNA and streptavidin QDs in solution form are reacted with the sample in sequence. For the final step, PMMA is lifted off with dichloromethane leaving the QD waveguide [52]. Additionally, creating multiple type QD devices through the method can take place by conjugating streptavidin coated QDs to biotinylated complementary DNA strands prior to assembly with a base DNA linked to the surface.

The second, rapid two-layer fabrication scheme [53] follows the initial PMMA and hydroxylation procedures and diverges at the point of monolayer assembly. Instead of MPTMS, we use 3′aminopropyltriethoxysilane (APTES), which presents an amine group at the surface after solution phase deposition. Carboxyl-conjugated QDs are covalently bound to the amine through a coupling reagent, namely 1-ethyl-3-(3′dimethylaminopropyl)-carbodiimide, and the waveguide in final form is revealed following PMMA removal. Here, several QD type waveguides may be formed via repetition of the steps for each different variety of nanocrystal (see Fig. 11). Pre-existing patterns are protected by PMMA coverage and specific placement of waveguides with respect to one another is achieved with the help of alignment marks.

As demonstration of the viability of multiple type QD waveguide fabrication, both fluorescence and atomic force microscopy images are presented in Fig. 12a, b. The devices show consistent, well-packed QD coverage in terms of emission and topology characteristics. To note, the overall resolution is limited by EBL and as such, extension of the device down to 10 ~ 20nm width is possible. EBL can also be replaced by high-resolution optical lithography for mass production.

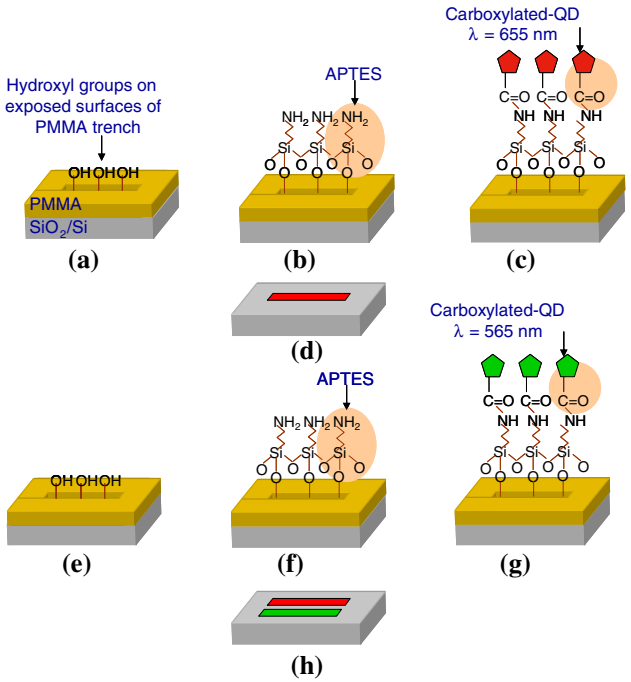

Fig. 11 Fabrication procedure for multiple type two-layer QD waveguides: (**a**) sample following e-beam lithography, development of PMMA and oxygen plasma treatment; (**b**) solution phase deposition of APTES self-assembled monolayer; (**c**) carboxylated QDs bound to amine terminal with coupling reagent; (**d**) sample after PMMA is stripped; (**e**)–(**f**) repeated process as in (**a**)–(**c**) with new PMMA layer; (**h**) sample after final PMMA removal

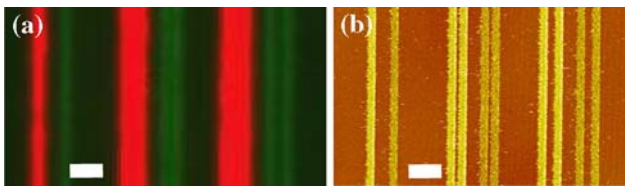

Fig. 12 (**a**) Fluorescence and (**b**) atomic force micrograph of a section of multiple QD type waveguide structures; waveguide width is 500 nm, scale bar is 2 μm

4.3 Test results

To test the devices, tapered fiber probes, created by chemical etching with 49% HF with a protection layer of isooctane, are aligned to the entry and exit waveguide edges. Rather than heat pulling, the etch process preserves the core diameter such that cladding material is removed at

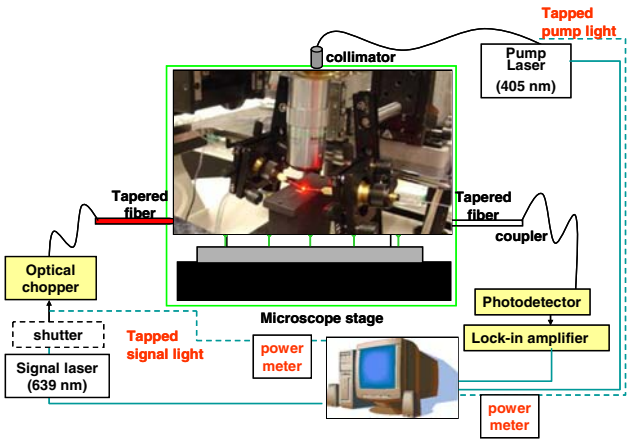

Fig. 13 Experimental setup for QD waveguide testing

the tip [54, 55]. The input probe is coupled to a 635 nm signal laser while the output is tied to a photodetector. A 405 nm pump light shines overhead onto the sample located on microscope stage. As described in the model section, the implementation of the waveguide relies on the pump to generate electron-hole pairs and enable gain in the QD. Then, the signal light triggers recombination of the e-h pairs, creating photons that cascade downstream inducing further stimulated emission.

To take the effect of laser power fluctuations into account, the pump and signal is tapped by 99/1 split ratio couplers and monitored by separate optical power meters with the majority of the light being directed to the sample. Then, the overall photodetector data may be normalized to the recorded laser variations. Moreover, placement of an optical chopper into the signal path prior to the probe stage combined with a lock-in amplifier following the photodetector improves the signal to noise ratio by focusing solely on changes in the transmitted modulated light. A diagram of the improved experimental setup, in Fig. 13, further clarifies the testing description.

Under the original setup, we can determine the waveguide performance by ramping the pump laser up and down, thereby varying the excitation rate of e-h pairs in the QDs. Using LabVIEW, photodetector measurements are logged periodically over time for four cycles with the signal on or off and the probes aligned to the substrate or waveguide. The measurements are taken for at least 5 min with 5 s between readings for each combination of pump, signal and probe settings. The contribution of the QDs is calculated by first averaging the points within each experimental setting. Then, we subtract the fluorescence measured from the sample when the signal laser is off from the data collected when the 635 nm light is on for the cases that the pump laser is active. Given that a lock-in amplifier is used for the measurement, the effect of QD fluorescence on the measured output signal is already minimal. In

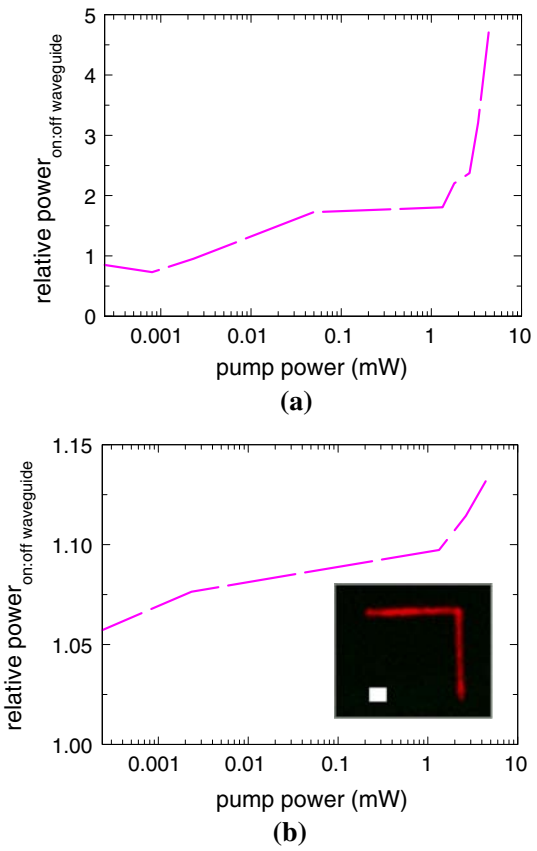

Fig. 14 Relative power data from 500 nm wide, (**a**) 10 μm straight and (**b**) 10 μm × 10 μm corner waveguides located on the same substrate. The inset of (**b**) is a fluorescent micrograph of the corner waveguide, scale bar is 1 μm

comparing the net signal on the waveguide to the substrate values, we take the ratio to determine the relative power provided by the device. As the ratio of on:off waveguide increases with higher pump power, we are able to see the effect of reduced absorption and potential gain.

The results for a 10 μm straight length and a 10 μm by 10 μm 90° corner devices fabricated with 655 nm emitting QDs, in Fig. 14a, b depict the expected trend of consistently higher output with pump excitation [56]. The straight device yields a higher ratio as the overall length is one half that of the corner and there is likely some loss at the junction point. Regardless, there is a noted improvement caused by the QD contribution in the output signal. With additional testing, we may further determine the loss and crosstalk behavior based on waveguide lengths and separation.

5 Conclusion

There is no question that discovering a low-loss, sub-diffraction waveguide that is easy to fabricate and integrate with existing circuitry is essential towards reducing the

footprint of photonic ICs while simultaneously increasing computing power. We have discussed several methods that compete to be the cornerstone of nanoscale optics, each with certain advantages and drawbacks. Whereas metal based processes introduce localized plasmons to transfer energy or alternatively act to inhibit 3D radiation in a slot waveguide or optical fiber, the process is inherently lossy due to the finite imaginary dielectric component. On the other hand, the nanoribbon, SOI high-index-contrast and photonic crystal-based structures are restricted by the difficulty in scaling the device while preserving the confinement behavior.

Our work on QD array waveguides attempts to address the underlying issues of sub-micrometer photonic components. However, further demonstrations are required to confirm mode confinement and coupling characteristics through experiments. Modeling of 2D QD coupling with pump and signal transmission effects may yield further proof. Undoubtedly, additional insights will lead to improved techniques for nanoscale energy transfer and the development for a host of commercially feasible, ultra-high density optical devices. Quite likely, a structure that combines the advantages of several different methods while minimizing the drawbacks will lead to commercial viability.

Acknowledgments We gratefully acknowledge funding from the National Science Foundation (NSF) ADVANCE program, and UW Royalty Research Fund. C.-J. Wang would like to thank the NSF Graduate and the Intel Foundation Ph.D. Fellowship Programs for financial support. Work was performed in part at the University of Washington Nanotech User Facility (NTUF), a member of the National Nanotechnology Infrastructure Network (NNIN), which is supported by the National Science Foundation.

References

1. J. Takahara, S. Yamagishi, H. Taki, A. Morimoto,T. Kobayashi, Optics Lett. **22**(7), 475 (1997)
2. J.R. Krenn, B. Lamprecht, H. Ditlbacher, G. Schider, M. Salerno, A. Leitner, F.R. Aussenegg, Europhys. Lett. **60**(5), 663 (2002)
3. D.F.P. Pile, T. Ogawa, D.K. Gramotnev, T. Okamoto, M. Haraguchi, M. Fukui, S. Masuo, App. Phys. Lett. **87**, 061106(2005)
4. M. Quinten, A. Leitner, J.R. Krenn, F.R. Aussenegg, Optics Lett. **23**(17), 133 (1998)
5. M.L. Brongersma, J.W. Hartman, H.A. Atwater, Phys. Rev. B **62**(24), 6356 (2000)
6. S.A. Maier, P.G. Kik, H.A. Atwater, S. Meltzer, E. Harel, B.E. Koel, A.A.G. Requicha, Nature Mater. **2**(4), 229 (2003)
7. L.A. Sweatlock, S.A. Maier, H.A. Atwater, J.J. Penninkhof, A. Polman, Phys. Rev. B **71**, 235408 (2005)
8. Maier S, IEEE J. Quantum Electron. **12**(6), 1214
9. R. Zia, M.D. Selker, P.B. Catrysse, M.L. Brongersma, J. Opt. Soc. Am. A **21**(12), 2442 (2004)
10. L. Chen, J. Shakya, M. Lipson, Opt. Lett. **31**(14), 2133 (2006)
11. D.F.P. Pile, T. Ogawa, D.K. Gramotnev, Y. Matsuzaki, K.C. Vernon, K. Yamaguchi, T. Okamoto, M. Haraguchi, M. Fukui, Appl. Phys. Lett. **87**, 261114 (2005)
12. F. Kusunoki, T. Yotsuya, J. Takahara, T. Kobayashi, Appl. Phys. Lett. **86**, 211101 (2005)
13. J. Takahara, F. Kusunoki, IEICE Trans. Electron **E90-C**(1), 87 (2007)
14. M.-S. Hu, H.-L. Chen, C.-H. Shen, L.-S. Hong, B.-R. Huang, K.-H. Chen, L.-C. Chen, Nat. Mat. **5**, 102 (2006)
15. J. Rybczynski, K. Kempa, A. Herczynski, Y. Wang, M.J. Naughton, Z.F. Ren, Z.P. Huang, D. Cai, M. Giersig, Appl. Phys. Lett. **90**, 021104 (2007)
16. S. Maier, Opt. Commun. **258**, 295 (2006)
17. M. Law, D.J. Sirbuly, J.C. Johnson, J. Goldberger, R.J. Saykally, P. Yang, Science **305**, 1269 (2004)
18. M. Law, J. Goldberger, P. Yang, Annu. Rev. Mater. Res. **34**, 83 (2004)
19. A. Ishimaru, *Electromagnetic Wave Propagation, Radiation, and Scattering*. (Prentice Hall, Upper Saddle River, New Jersey, 1991)
20. K.K. Lee, D.R. Lim, L.C. Kimmerling, J. Shin, F. Cerrina, Opt. Lett. **26**(23), 1888 (2001)
21. C.A. Barrios, V.R. Almeida, R. Panepucci, M. Lipson, J. Lightwave Technol. **21**(10), 2332 (2003)
22. Q. Xu, V.R. Almeida, R. Panepucci, M. Lipson, Opt. Lett. **29**(14), 1626 (2004)
23. W. Bogaerts, R. Baets, P. Dumon, V. Wiaux, S. Beckx, D. Taillaert, B. Luyssaert, J. Van Campenhout, P. Bienstman, D. Van Thourhout, J. Lightwave Technol. **23**(1), 401 (2005)
24. J.D. Joannopoulos, R.D. Meade, J.N. Winn, *Photonic Crystals*. (Princeton University, Princeton, NJ, 1995)
25. S.G. Johnson, P.R. Villeneuve, S. Fan, J.D. Joannopoulos, Phys. Rev. B **62**(12), 8212 (2000)
26. M. Notomi, A. Shinya, S. Mitsugi, E. Kuramochi, H.-Y. Ryu, Opt. Exp. **12**(8), 1551 (2004)
27. S. Vyawahare, S. Eyal, K.D. Mathews, S.R. Quake, Nano Lett. **4**(6), 1035 (2004)
28. W.C.W. Chan, S. Nie, Science **281**, 2016 (1998)
29. M. Bruchez Jr., M. Moronne, P. Gin, S. Weiss, A.P. Alivisatos, Science **281**, 2013 (1998)
30. R. Dingle, C.H. Henry, U.S. Patent 3,982,207, 21 Sept 1976
31. N.N. Ledentsov, M. Grundmann, F. Heinrichsdorff, D. Bimberg, V.M. Ustinov, A.E. Zhukov, M.V. Maximov, Z.I. Alferov, J.A. Lott, IEEE J. Quantum Electron. **6**(3), 439 (2000)
32. V.M. Ustinov, A.E. Zhukov, A.Y. Egorov, N.A. Maleev, *Quantum Dot Lasers*. (Oxford University Press, Oxford, 2003)
33. H. Cao, J.Y. Xu, W.H. Xiang, Y. Ma, S.-H. Chang, S.T. Ho, G.S. Solomon, Appl. Phys. Lett. **76**(24), 3519 (2000)
34. O. Benson, Y. Yamamoto, Phys. Rev. A **59**(6), 4756 (1999)
35. K.J. Vahala, IEEE J. Quantum Electron. **24**(3), 523 (1988)
36. M. Ohtsu, K. Kobayashi, T. Kawazoe, T. Yatsui, IEEE J. Quantum Electron. **8**(4), 839 (2002)
37. T. Kawazoe, K. Kobayashi, S. Sangu, M. Ohtsu, J. Microsc. **209**, 261 (2003)
38. C.B. Murray, C.R. Kagan, M.G. Bawendi, Annu. Rev. Mater. Sci. **30**, 545 (2000)
39. M.G. Bawendi, P.J. Carroll, W.L. Wilson, L.E. Brus, J. Chem. Phys. **96**(2), 946 (1992)
40. B.R. Fisher, H.-J. Eisler, N.E. Stott, M.G. Bawendi, J. Phys. Chem. B **108**, 143 (2004)
41. A.Y. Nazzal, X. Wang, L. Qu, W. Yu, Y. Wang, X. Peng, M. Xiao, J. Phys. Chem. B **108**, 5507 (2004)
42. V.I. Klimov, A.A. Mikhailovsky, S. Xu, A. Malko, J.A. Hollingsworth, C.A. Leatherdale, H.-J. Eisler, M.G. Bawendi, Science **290**, 314 (2000)
43. L.-W. Wang, M. Califano, A. Zunger, A. Franceschetti, Phys. Rev. Lett. **91**(5), 056404, (2003)
44. P. Guyot-Sionnest, M. Shim, C. Matranga, M. Hines, Phys. Rev. B **60**(4), R2181, (1999)

45. V.I. Klimov, A.A. Mikhailovsky, D.W. McBranch, C.A. Leatherdale, M.G. Bawendi, Science **287**, 1011 (2000)
46. C.-J. Wang, L.Y. Lin, B.A. Parviz, IEEE LEOS 18th Annual Meeting Proc., 177 (2005)
47. C.-J. Wang, L.Y. Lin, *SPIE Optics East*, Proceedings of SPIE, vol. 5593. Nanosensing: Materials and Devices, 378 (2004)
48. M. Asada, Y. Miyamoto, Y. Suematsu, IEEE J. Quantum Electron. **22**(9), 1915 (1986)
49. C.-J. Wang, L.Y. Lin, B.A. Parviz, IEEE J. Quantum Electron. **11**(2), 500 (2005)
50. L. Huang, C.-J. Wang, L.Y. Lin, Opt. Lett. **32**(3), 235 (2007)
51. C.-J. Wang, L.Y. Lin, B.A. Parviz, IEEE/LEOS Int. Optical MEMS Conf. Proc. **24** (2004)
52. W. Hu, K. Sarveswaran, M. Lieberman, G.H. Bernstein, IEEE Trans. Nanotech. **4**, 312 (2005)
53. C.-J. Wang, L.Y. Lin, B.A. Parviz, CLEO/QELS Conf. Proc. (2006)
54. S.J. Bukofsky, R.D. Grober, App. Phys. Lett. **71**(19), 2749 (1997)
55. P. Lambelet, A. Sayah, M. Pfeffer, C. Philipona, F. Marquis-Weible, App. Opt. **37**(31), 7289 (1998)
56. C.-J. Wang, L. Huang, B.A. Parviz, L.Y. Lin, Nano Lett. **6**(11), 2549 (2006)